TRANSIENT ANALYSIS OF A FLYWHEEL BATTERY CONTAINMENT DURING A FULL ROTOR BURST EVENT

B. J. Hsieh and R. F. Kulak
Reactor Engineering Division
Argonne National Laboratory
Argonne, Illinois

J. H. Price and B. T. Murphy
Center for Electromechanics
The University of Texas at Austin
Austin, Texas

ABSTRACT

Flywheels are being developed for use in an Advanced Locomotive Propulsion System (ALPS) targeted for use in high speed passenger rail service. The ALPS combines high performance, high speed gas turbines, motor/generators and flywheels to provide a light-weight, fuel-efficient power system. Such a system is necessary to avoid the high cost of railway electrification, as is currently done for high speed rail service (>100 mph) since diesels are too heavy. The light-weight flywheel rotors are made from multilayered composite materials, and are operated at extremely high energy levels. Metal containment structures have been designed to enclose the rotors and provide encapsulation of the rotor during postulated failure events. One such event is a burst mode failure of the rotor in which the composite rim is assumed to burst into debris that impacts against the containment. This paper presents a finite element simulation of the transient structural response of a subscale metal flywheel containment structure to a rotor burst event.

INTRODUCTION

A subscale ALPS flywheel has been constructed by the University of Texas Center for Electromechanics (CEM) for spin testing. These tests have been designed to serve a number of purposes, including evaluation of the performance of the flywheel containment. Containment testing will be accomplished by intentionally failing the flywheel at a predetermined speed using a shape charge aligned axially over one end of the rim of the rotor. Among the issues to be addressed are (1) the overall ability of the containment to withstand a flywheel burst event, (2) the strength of the joint between the cylindrical wall and the end plates (end caps), and (3) the validity of the computer models and codes that are being used to evaluate flywheel safety.

The subscale tests have been designed using a rotor diameter that is about one-third of the full-scale locomotive flywheel diameter. The nominal maximum spin velocity is such that the tip speed of the subscale rotor is equal to that of the full-scale rotor with a stored energy of 500 MJ.

The next section describes the key features of the current containment design. This is followed by a description of the debris loading model that was used in the simulation. Next, the finite element model and simulation results are presented. Finally, a summary and conclusions are presented.

CONTAINMENT DESIGN

The containment is designed in three pieces as shown in Fig. 1. The casing is a cylindrical shell made from 304 stainless steel with threads at both ends. End caps are threaded onto each end of the casing. Table 1 provides some of the key parameters for the subscale flywheel.

Table 1. Subscale Flywheel Parameters

Containment Material	Type 304 Stainless Steel
Flywheel Rim Outer Radius	8.04 inches (0.204 m)
Flywheel Rim Inner Radius	6.50 inches (0.165 m)
Flywheel Rim Length	12.13 inches (0.308 m)
Containment Inner Radius	8.17 inches (0.207 m)
Containment Thickness	1.25 inches (0.0318 m)

Figure 2 is a schematic that shows the subscale flywheel and containment inside a spin pit. Further details are in Herbst et al.

DEBRIS LOADING MODEL

The loading models developed to analyze containment response following flywheel failure are described by Pichot et al. These models use fundamental energy and momentum principles to calculate the radial, axial and torsional loading on the containment wall and end plates. Because of uncertainties associated with the kinetics of the flywheel debris following a rotor burst, two separate models were developed. In the first model, debris deflection model, the debris is assumed to impact the inside wall of the containment and to be immediately deflected axially without any accumulation on the wall. The second model, debris accumulation model, assumes that all of the fragments pack into a debris bed against the wall without any axial deflection.

The two different loading scenarios have been used to analyze the capability of the ALPS containment to withstand a flywheel burst. To some extent, the two extremes that these models represent provide bounds for analyzing the containment response. The debris deflection model tends to produce an impulsive loading that maximizes the magnitude of the axial loading. On the other hand, the debris accumulation model tends to produce longer duration loading and maximizes the torque on the containment. In the pretest blind calculations for the subscale test, the entire rotor is assumed to fail instantaneously when the shape charge is triggered.

All of the following computer simulations used the debris accumulation model because it more closely represents the real case. Using this model, time dependent pressure histories were determined for the following spin speeds: 33,550 rpm, 28,630 rpm and 23,710 rpm. The pressure is applied to the inner surface of the casing; no loading is applied to the end plate. Figure 3 shows the debris loading histories for the three spin speeds. The shape of the pressure history for all three load cases is similar. It is seen that for the spin speed of 33,550 rpm, the pressure rises to a maximum value of 21,070 psi (145 MPa) during the first 1.2 μs and then decays to 570 psi (4 MPa) at 3 ms. For the next slower speed, 28,630 rpm, the maximum pressure of 15,380 psi (106 MPa) occurs at 1.2 μs, and for the slowest speed, 23,710 rpm, the maximum pressure is 10,540 psi (73 MPa) at 1.2 μs.

NUMERICAL SIMULATION

A numerical simulation of the subscale containment was performed using the STRAW computer code (Kennedy et al.) developed at Argonne National Laboratory for the fast transient response of reactor components. STRAW is a nonlinear finite element code that uses explicit time integration, which is computationally efficient for these problems. The code treats both geometric and material nolinearities. Nonlinear continuum and contact elements were used in the simulations. A computational time step of 0.15 μs was used for all simulations.

Threaded Joint Model

An axisymmetric finite element model (Fig. 4) composed of two disjoint meshes was generated: one mesh represented the end plate and the other the casing. Note, only one-half of the length of the containment is modeled, that is, one end plate and one-half of the casing. To catch the details of the threads, the elements had to be much smaller than the elements used in the monolithic model. The number of nodes and elements were 2,175 and 1,973, respectively. The threaded interface between the end plate and the casing is modeled with sufficient detail to capture the contact mechanics within the threaded joint. The gap between the threads can be seen in Fig. 5, which shows the confinement before debris loading. A contact algorithm is used to treat the interactions in the threaded joint.

Here the boundary conditions applied to the model are described. The test setup is such that the upper end plate is attached to a collar in the mounting plate and the lower end plate is free; however, it does have a steel plug in the large shaft opening. Since the model only treats one-half of the length of the containment and the boundary conditions at each end are different, the following boundary conditions were chosen as an average. The nodes along the horizontal symmetry plane of the casing were restricted to radial translational motion only. Thus, these boundary conditions represent a horizontal symmetry plane. For the end plate, the following nodal constraints were applied to the nodes along the inner diameter, which is where the upper end plate would be attached to the mounting plate. These nodes are constrained from moving in the negative radial (inward) direction, but are allowed to move in the positive radial (outward) direction and in the axial direction. As mentioned above, a contact algorithm was used to handle the impact/contact in the threaded joint.

The material properties used in the analysis are those for Type 304 stainless steel and are given in Table 2 below.

Table 2. Material Properties for Type 304 Stainless Steel

Young's Modulus	26.8×10^6 psi (185.0×10^9 Pa)
Poisson's Ratio	0.27
Yield Strength	30.5×10^3 psi (210.0×10^6 Pa)
Uniform Elongation	25%
Ultimate Strength	72.5×10^3 psi (500.0×10^6 Pa)
Tangent Modulus	1.68×10^5 psi (1.16×10^9 Pa)

An isotropic elastoplastic material model with a von Mises yield surface and linear hardening was used to model the Type 304 Stainless Steel.

Results for Spin Speed of 33,550 rpm

The first simulations were done for a spin speed of 33,550 rpm. Initially, the debris loading on the inside surface of the casing propagates as waves through the casing wall causing the casing to move outward. Then, the casing contacts the end plate at the seal collar and first thread causing localized plastic deformation.

At 0.750 ms into the burst event, the containment has undergone extremely large deformations as illustrated in Fig. 6. The casing continues to deform outward and to transfer radial and axial loads to the end plate. As the casing bulges outward, it continues to pull the end cap downward. The gap is still on the topside of the casing threads. Note, the thread engagement has been greatly reduced. The casing is seeing a maximum effective plastic strain of 21% on its inner and outer surfaces. Part of the end plate is still in the elastic regime.

Eventually, the outward motion of the casing slows and the downward moving end plate closes the gap. The contact between the casing threads and the end-cap threads stops the downward motion of the cap. This occurs around 1.08-1.10 ms into the burst event. No additional significant plasticity occurs beyond this time. After this time, the end plate rebounds off the casing causing the gap to return to the topside of the casing threads. At the end of the simulation (3.0 ms), the casing and end plate are as shown in Fig. 7. The maximum effective strain of 25% occurs on the inside surface of the casing at the mid section.

Displacement, velocity, and acceleration histories are shown in Figs. 8-10, respectively. The displacement histories of the outer surface of the casing at the mid-section (i.e., point "A" of Fig. 4) and the outer surface of the end-cap at the top of the collar (i.e., point "B" of Fig. 4) are shown in Fig. 8. It is seen that the casing moves outward to a peak displacement of 2 in at 1.00 ms and, subsequently, continues to vibrate with a small amplitude. The maximum downward movement of the end plate is 1.2 in at 1.4 ms. The mid-section of the casing reaches a peak velocity of 3,000 in/sec at 0.45 ms (Fig. 9). Figure 10 shows that the peak acceleration of 349×10^3 g occurs at 0.03 ms after initiation of debris loading.

Figure 11 shows the evolution of the containment's kinetic energy and the strain energy. The kinetic energy reaches a peak value of 1.82×10^5 lb_f-in (0.02 MJ) at about 0.4 ms and then decays to zero. Note, the kinetic energy accounted for here is the kinetic energy of the deforming containment caused by debris impacting normally to the inside surface of the casing. The tangential component of the debris loading imparts large rotational motion (kinetic energy) to the containment. However, this aspect of the burst event is not taken into account with the axisymmetric model; a three-dimensional model is needed to capture the rotational motions. The strain energy reaches a peak value of 6.16×10^5 lb_f-in (0.07 MJ) at 1.3 ms and remains at that level, since it is mostly the energy due to the large plastic deformations in the casing and end plate. Note, since only half of the containment was modeled, the energies should be doubled for the full containment, that is, the peak kinetic energy would be 3.63×10^5 lb_f-in (0.04 MJ) and the peak strain energy would be 1.230×10^6 lb_f-in (0.14 MJ). It is interesting that the kinetic energy of the subscale flywheel at a spin speed of 33,550 rpm is 5.4 MJ; thus, only about 2.6% of the energy is absorbed by the deformed containment.

Results for Spin Speeds of 28,630 rpm and 23, 710 rpm

Additional load cases were run with the threaded joint model. Some results are presented here. It was found that the deformations are much less than those at 33,550 rpm. The maximum effective plastic strain is reduced from 25% down to 14% at 28,630 rpm. For the slowest speed (23,710 rpm) the maximum effective plastic strain is only 4.5%.

SUMMARY AND CONCLUSIONS

A finite element simulation of the transient response of a flywheel battery containment to debris loading was performed. A finite element model of the containment was developed that included the details of the threaded joint between the casing and end plates. The debris accumulation model was used to calculate the pressure loading applied to the casing. The largest plastic strains occurred in the mid section of the casing. Also, the model captured the impacts and oscillations between the end plate and the casing.

The simulations with the threaded joint model yielded the following conclusions:

(1) The fabricated containment can probably resist loading from a flywheel burst at 33,550 rpm. However, the effective plastic strain has reached the value for uniform elongation for the type 304 stainless steel and there may not be any margin beyond this point. In addition, the deformation is substantial and thread disengagement is impending.

(2) Analysis showed that when detailed modeling of the threads was included, the large deformations of the joint created unequal loading of the threads and unequal gaps between them. However, the thread design was robust and failure of the material would not occur in the threaded region As pointed out above, disengagement of the threads was impending.

(3) By far the largest plastic strains were calculated to occur near the mid-section of the containment. These strains were relatively independent of the boundary condition imposed at the inner diameter of the end plates.

(4) At a spin speed of 28,630 rpm, the containment can resist a flywheel burst event. The maximum effective plastic strains of 14% are well below the uniform elongation value and the deformations are moderate, which preclude disengagement of the threads.

ACKNOWLEDGMENTS

Work reported in this paper was performed under the sponsorship of the U.S. Department of Transportation Federal Railroad Administration, the State of Texas Match Pool, the Defense Advanced Research Projects Agency (DARPA), and the Southern Coalition for Advanced Transportation (SCAT).

REFERENCES

Kennedy, J.M., Belytschko, T.B. and Schoberle, D.F., 1980, "A Quasi-Eulerian Fluid-Structure Code for Simulation of High-Pressure Transients in Core Components," *Nuclear Technology*, Vol. 51, No. 3, pp. 290-302.

Herbst, J.D., Manifold, S.M., Murphy, B.T., Price, J.H., Thompson, R.C., Walls, W.A., Alexander, A. and Twigg, K., 1998, "Design, Fabrication, and Testing of 10 MJ Composite

Flywheel Energy Storage Rotors," to be presented at the 1998 SAE Aerospace Power Systems Conference, April 21-23, 1998.

Pichot, M. A., Kramer, J. M., Thompson, R. C., Hayes, R. J. and Beno, J. H., 1997, "The Flywheel Battery Containment Problem," *SAE Technical Paper Series*, Book Number: SP-1243, Document Number: 970242.

Figure 1. Containment shroud and end plates.

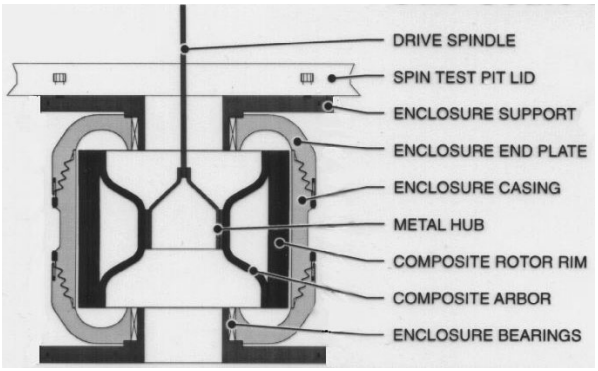

Figure 2. Schematic of rotor and containment.

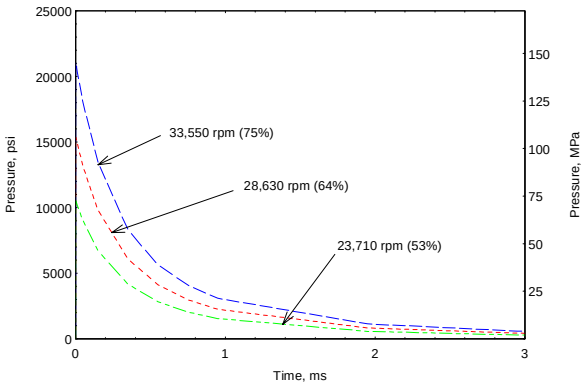

Figure 3. Debris loading histories for spin speeds of 33,550 rpm, 28,630 rpm, and 23,700 rpm.

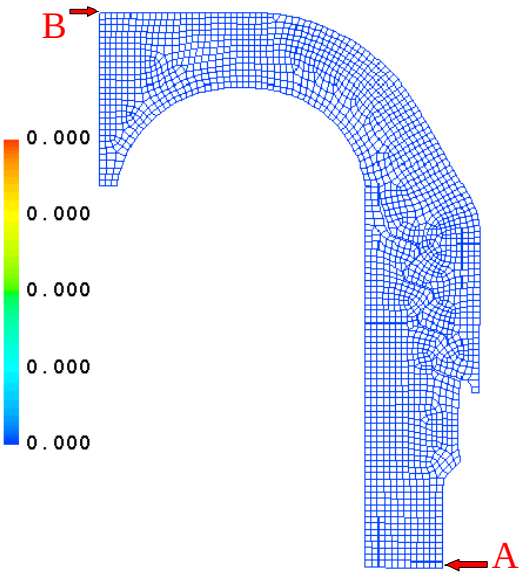

Figure 4. Axisymmetric finite element model composed of two disjoint meshes: one mesh represents the end plate and the other the casing. The number of nodes and the number of elements are 2,175 and 1,973, respectively.

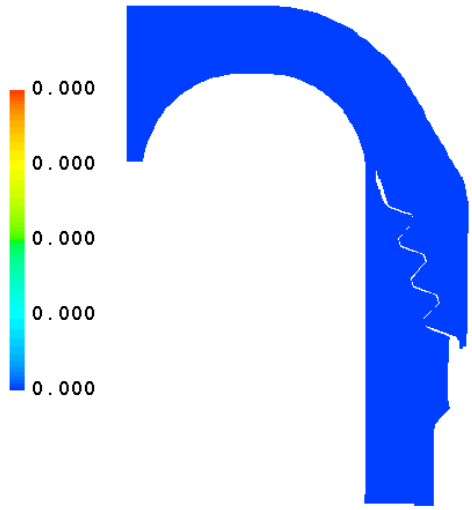

Figure 5. Configuration of containment prior to debris loading. The gap in the threaded joint is shown.

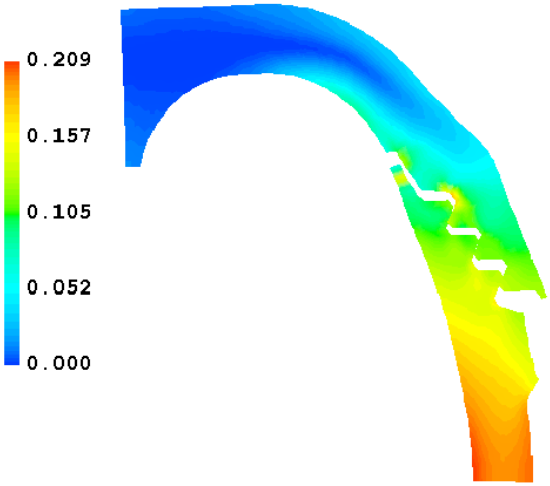

Figure 6. Deformed configuration of casing and end plate at 0.750 ms after burst loading. Large gaps have developed in the threaded joint. Effective plastic strain is shown.

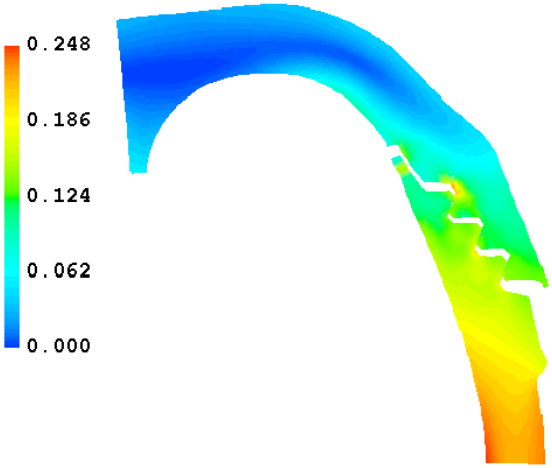

Figure 7. Deformed configuration and distribution of total plastic strain at 3.000 ms after the burst event.

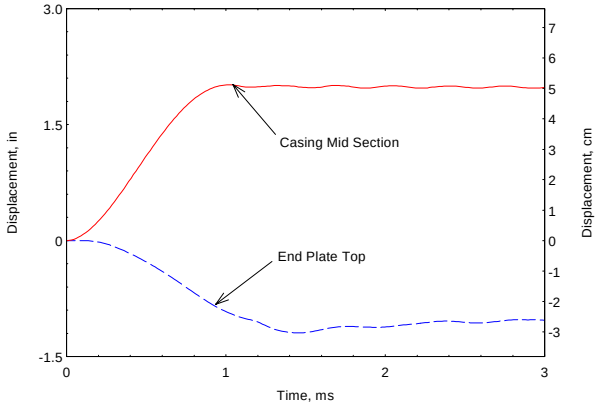

Figure 8. Radial displacement history of the midsection of the casing (outside surface) and axial displacement history of the top of the end plate (outside surface) for a spin speed of 33,550 rpm.

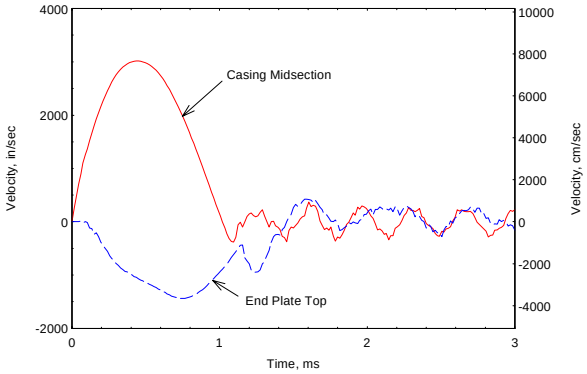

Figure 9. Radial velocity history of the midsection of the casing (outside surface) and axial velocity history of the top of the end plate (outside surface) for a spin speed of 33,550 rpm.

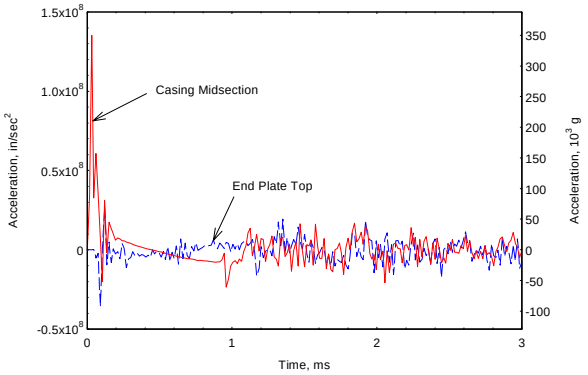

Figure 10. Radial acceleration history of the midsection of the casing (outside surface) and axial acceleration history of the top of the end plate (outside surface) for a spin speed of 33,550 rpm.

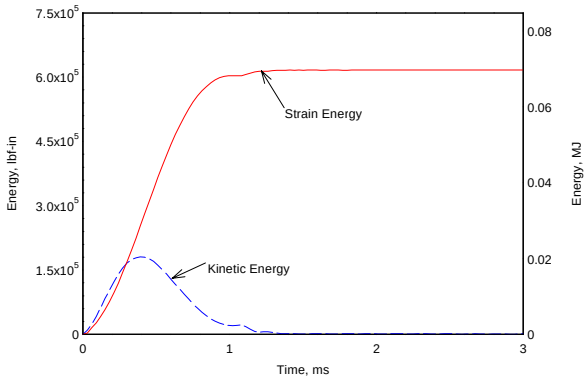

Figure 11. Evolution of containment strain and kinetic energies for a 33,550 rpm burst event.